Journal of Materials Chemistry A

ROYAL SOCIETY OF CHEMISTRY

PAPER

Cite this: *J. Mater. Chem. A*, 2026, **14**, 16767

Illumination-boosted capacitance with $NiFe_2O_4$: design and performance of symmetric and asymmetric photo-powered supercapacitors with self-generated voltage

Shekoufeh Pira,[a] Mohamad Mohsen Momeni *[a] and Fuxiang Zhang [b]

Received 17th December 2025
Accepted 16th March 2026

DOI: 10.1039/d5ta10294d

rsc.li/materials-a

The demand for renewable energy requires efficient methods of energy generation and storage. Photo-powered supercapacitors (PPSCs) store more charge when illuminated, supporting the sustainability of the energy supply. PPSCs require active materials capable of both charge separation and storage. This work describes symmetric and asymmetric PPSC configurations using nickel ferrite ($NiFe_2O_4$) as a photoelectrode. $NiFe_2O_4$ is a spinel oxide valued for its applications in photocatalysis and supercapacitors. $NiFe_2O_4$ nanoparticles, prepared by co-precipitation and calcined at different temperatures from 400 to 800 °C, exhibit temperature-dependent structure and morphology; higher calcination temperatures produce larger, more aggregated particles. Based on galvanostatic charge–discharge (GCD) measurements, the NF-600 electrode (calcined at 600 °C) exhibits the highest specific capacitance. Under illumination with a current density of 0.03 mA cm^{-2}, NF-600 achieves a specific capacity of 422.88 mA h g^{-1}, approximately 1.34 times the value obtained in the dark (314.96 mA h g^{-1}) at room temperature. The NF-600 photoelectrode was used to fabricate both symmetric and asymmetric photo-powered supercapacitors. The results indicate that the asymmetric device exhibited superior performance. Two of the devices generated a self-induced voltage without external bias. Under illumination, both devices showed improved electrochemical performance, including increased capacitance and energy density. The asymmetric device demonstrated better performance and enhanced cycling stability compared to the symmetric device. This work presents a simple PPSC fabrication method using nickel ferrite to enhance sustainable charge storage in future energy devices.

1. Introduction

Given the increasing effects of climate change and environmental pollution, global energy demand continues to rise. Developing greener and more sustainable concepts for energy conversion and storage has become a key objective.[1] The ability to repeatedly recharge an energy storage system (ESS) without relying on fossil fuels is desirable for achieving a low-carbon, sustainable society.[1,2] This goal is essential due to the rapid growth of portable devices, including wearable electronics, whose energy requirements are continually increasing. In practice, solar energy is often used as an auxiliary power source to extend the lifespan of these devices. Solar energy is one of the most important renewable and sustainable resources. Recently, photo-chargeable electrical energy storage systems, capable of both converting and storing solar energy, have attracted considerable attention. Semiconductor materials are integrated into photo-powered supercapacitors (PPSCs) to enable simultaneous utilization of photoactive and capacitive properties, thereby improving both solar energy harvesting and energy storage.[3,4] The advent of modern wearable electronics has driven the development of multifunctional advanced energy devices that demonstrate strong energy storage performance, environmental adaptability, and robust mechanical durability.[3–6] Flexible photo-powered supercapacitors (FPPSCs) have emerged as a promising category of portable power devices, offering faster charge–discharge dynamics, higher power density, and longer cycle life.[5]

Transition metal oxides (TMOs), especially mixed oxides in spinel form (MTMOs), are a major source of stable supercapacitor materials due to their chemical composition and synergistic effects.[7–9] MFe_2O_4 ferrites (M = Co, Ni, Mn, Cu, Zn, *etc.*) are important supercapacitor electrodes as they are inexpensive, non-hazardous, and widely available.[8] Ferrite nanostructures, with their large surface area and high chemical stability in aqueous electrolytes, have recently attracted attention as efficient candidates for supercapacitors.[10–12] The high

[a]*Department of Chemistry, Isfahan University of Technology, Isfahan 84156-83111, Iran. E-mail: mm.momeni@cc.iut.ac.ir*

[b]*State Key Laboratory of Catalysis, Dalian Institute of Chemical Physics, Chinese Academy of Sciences, Dalian National Laboratory for Clean Energy, 116023 Dalian, P. R. China*

capacitance of MFe_2O_4 electrodes is largely due to redox reactions, while their electric double-layer (EDL) capacitance is comparatively modest. In addition, MFe_2O_4 exhibits significant visible light absorption and good electrical conductivity. Metal ferrites have been reported to show promising photocatalytic activity, benefiting from enhanced visible light utilization, favorable band gaps (around 1.75 eV), diverse morphologies, and distinct optical and electronic properties. Consequently, semiconductor spinel ferrites are considered promising candidates for the development of efficient and cost-effective photoelectrochemical (PEC) systems. Nickel ferrite ($NiFe_2O_4$) has an inverted structure, with Ni^{2+} in octahedral sites and Fe^{3+} in both octahedral and tetrahedral sites.[7–13] This arrangement facilitates electron transfer and the formation of redox-active centers on the surface. Owing to its excellent electrochemical stability, it is suitable for electrocatalysis, Li-ion batteries, and supercapacitors.[13] As a faradaic electrode, $NiFe_2O_4$ is popular because of its abundance, low cost, and environmental friendliness. Its electrochemical properties depend on its structure and morphology, which can be adjusted by synthesis parameters. In addition, nickel ferrite is considered a potential visible light photocatalyst for the degradation of organic pollutants and water oxidation, as it has a band gap of about 1.72 eV, is non-toxic, and can be easily separated magnetically. Since a large portion of sunlight is in the visible range (approximately 43% between 400 and 700 nm), supercapacitors that are active under visible light are highly desirable.[7–14]

In this study, $NiFe_2O_4$ nanostructures were synthesized *via* co-precipitation and calcined at 400–800 °C to investigate the effects of thermal treatment on their structural, optical, and photoelectrochemical properties. While the synthesis route is well-known,[15–17] this work establishes a clear correlation between calcination temperature, defect chemistry, and photo-assisted charge storage. The sample calcined at 600 °C showed the highest specific capacity, which increased significantly under light, highlighting pronounced photo-enhanced performance. $NiFe_2O_4$/ITO electrodes were then used to fabricate flexible symmetric and asymmetric photo-powered supercapacitors, which exhibited self-charging behavior under illumination. These results demonstrate the potential of thermally tuned $NiFe_2O_4$ as a dual-function photoelectrode in integrated photo-powered energy storage systems.

2. Experimental

2.1. Materials

All chemicals used in this study were of analytical grade and used as received without further purification. Ferric chloride ($FeCl_3 \cdot 6H_2O$) and nickel chloride ($NiCl_2 \cdot 6H_2O$) were purchased from Riedel-de Haën, and oleic acid was obtained from Merck. Distilled water and ethanol were used throughout the experiments.

2.2. Preparation of nickel ferrite nanoparticles

$NiFe_2O_4$ nanoparticles were synthesized *via* a co-precipitation method adapted from previous reports.[18] In brief, aqueous solutions of ferric chloride and nickel chloride were prepared in distilled water, followed by the addition of 5 mL oleic acid as a surfactant. NaOH solution was gradually introduced under continuous stirring until the pH reached 10. The resulting mixture was then heated at 80 °C for 60 minutes and cooled to room temperature. The precipitate was washed four times with distilled water and ethanol to remove residual sodium and chloride ions, and surfactant molecules. After washing, the material was centrifuged and dried at 100 °C for 3 h. The dried powder was subsequently calcined at 400, 500, 600, 700, and 800 °C for 10 h to produce samples labeled NF-400, NF-500, NF-600, NF-700, and NF-800, respectively (Fig. 1). The detailed formation pathway and proposed ferritization mechanism of $NiFe_2O_4$ including the co-precipitation of metal hydroxides and their subsequent transformation into spinel ferrite during alkaline heat treatment, are presented in the supplementary material.

2.3. Material characterization

Phase composition, purity, and crystal structure of the synthesized samples were determined by X-ray diffraction (XRD) using a Philips Pert system equipped with a Cu Kα source (λ = 0.154 nm, 60 kV). Data was collected over the 2θ range of 5° to 80°. Morphology was characterized by field-emission scanning electron microscopy (FE-SEM) on a QUANTA FEG 450 system, equipped with energy-dispersive X-ray spectroscopy (EDS). Additional structural information was corroborated by transmission electron microscopy (TEM, JEOL JMT-2100F). Surface composition and oxidation states were analyzed by X-ray photoelectron spectroscopy (XPS; ESCALAB 250XI, Thermo Fisher Scientific) with a monochromated Al-Kα source.

2.4. Electrochemical measurements

Electrochemical measurements were performed with an SAMA500 potentiostat/galvanostat. In a three-electrode configuration, the working electrode was $NiFe_2O_4$/ITO, and the counter electrode was a Pt plate measuring 10 mm by 10 mm. A saturated Ag/AgCl electrode served as the reference electrode, with a 2 M KCl electrolyte. When connected to the potentiostat, an LED lamp with an intensity of 100 mW cm^{-2} was used to simulate solar irradiation for optoelectronic performance evaluation. The electrochemical tests conducted included cyclic voltammetry (CV), galvanostatic charge–discharge (GCD), and electrochemical impedance spectroscopy (EIS). In EIS measurements, the open-circuit potential frequency ranged from 10^5 to 10^{-1} Hz. CV experiments were performed over a potential window of −0.4 to 0.4 V at various scan rates. GCD tests were carried out within a fixed potential window of 0.8 V at different current densities.

2.5. Preparation of PVA/KCl gel electrolyte

An aqueous solution of polyvinyl alcohol (PVA) was prepared by dispersing 3 g of PVA in 30 mL of deionized water. The mixture was stirred at 60 rpm for 6 hours at room temperature until a clear, transparent solution was obtained. Then, 15 mL of KCl

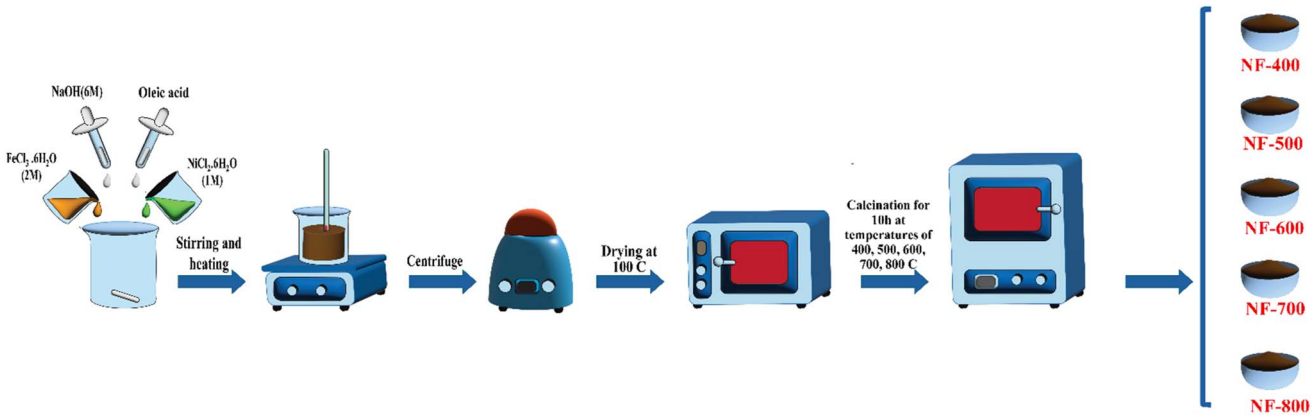

Fig. 1 Schematic representation of the synthesis processes for the various samples.

(2 M) solution was added dropwise to the initial solution and stirred for a further 1 hour to obtain a homogeneous gel.

2.6. Fabrication of two-electrode photo-powered supercapacitors (PPSCs)

In addition, two-electrode studies used $NiFe_2O_4$/ITO as photoelectrodes. Both symmetric and asymmetric photo-powered supercapacitors were assembled. For the symmetric configuration, two $NiFe_2O_4$/ITO electrodes exhibiting the best photoelectrochemical performance (sample NF-600) were placed face-to-face with a separator and properly sealed. For the asymmetric configuration, one electrode was fabricated from the optimal $NiFe_2O_4$/ITO sample, while the other electrode consisted of a flexible graphite foil. The assembly steps for the symmetric device were similarly followed for the alternating arrangement. A PVA–KCl gel electrolyte was prepared and

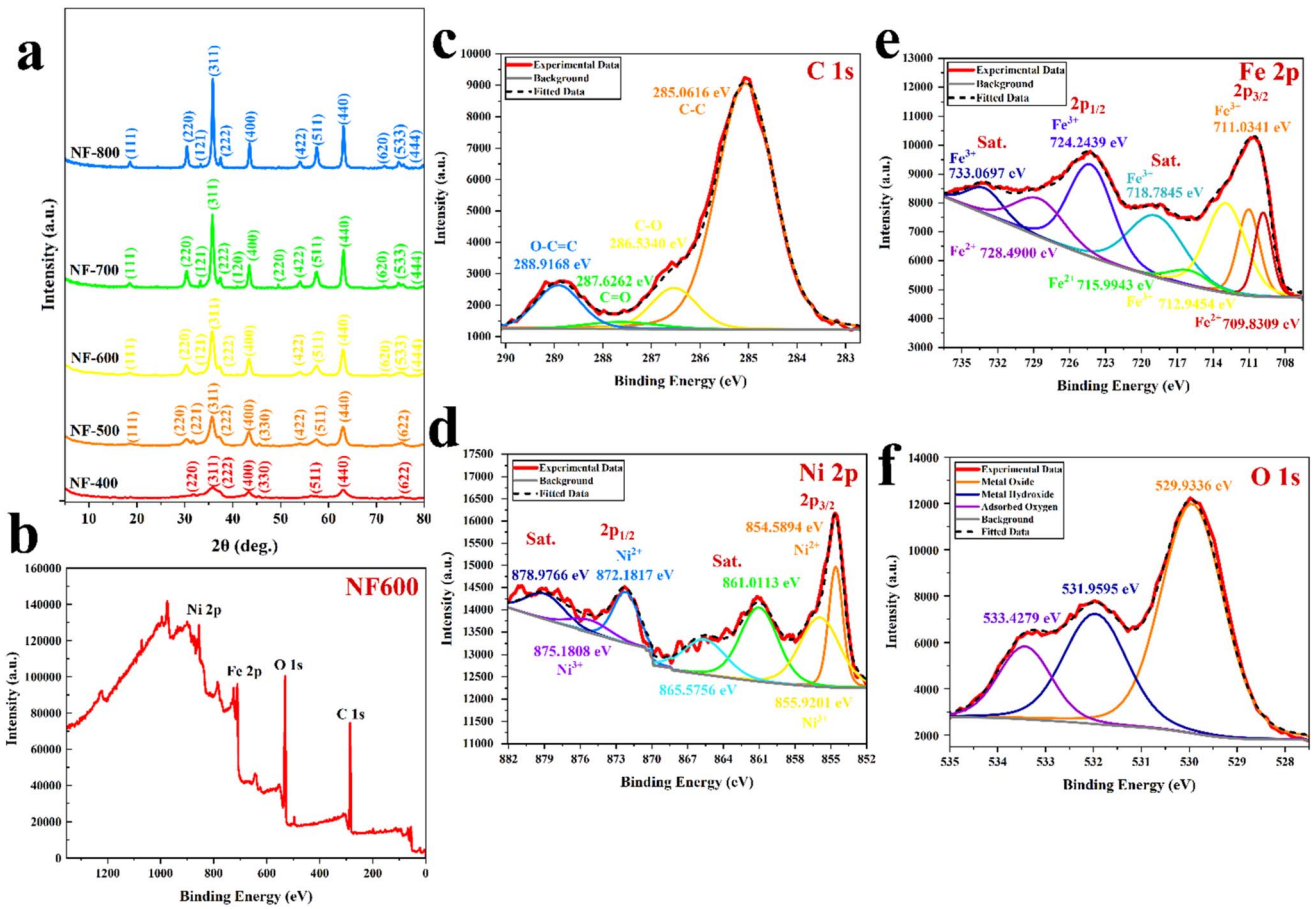

Fig. 2 (a) XRD patterns of prepared samples. (b) XPS survey spectrum of $NiFe_2O_4$ nanoparticles (sample NF-600). High-resolution core-level XPS spectra of (c) C 1s, (d) Ni 2p, (e) Fe 2p, and (f) O 1s.

employed between the two electrodes in the assembled supercapacitors, where the gel acted as both the electrolyte and the separator within the devices. To evaluate how illumination affects device performance, including energy storage capabilities and efficiency, the electrochemical behavior of the photo-powered supercapacitors was characterized by cyclic voltammetry (CV), galvanostatic charge–discharge (GCD), and electrochemical impedance spectroscopy (EIS) under both dark and light conditions.

3. Results and discussion

3.1. Characterizations of prepared samples

X-ray diffraction (XRD) analysis was performed to assess the samples' crystalline structure and phase purity. Fig. 2a shows the diffraction pattern of $NiFe_2O_4$ nanostructures calcined at 400–800 °C. Eight strong reflections appear at 2θ values of 18.4°, 30.3°, 35.6°, 43.4°, 54.03°, 57.5°, 63.00° and 74.6°, corresponding to the planes (111), (220), (311), (400), (422), (511), (440) and (533), respectively. The observed pattern is fully consistent with the JCPDS card no. 01-074-2081.[19–22] The absence of extraneous peaks indicates no secondary phases and confirms the high purity of the prepared samples. The broad diffraction features indicate nanoscale particle dimensions. As the calcination temperature increases, the peak intensities become more pronounced while the full width at half maximum (FWHM) decreases, indicating enhanced crystallinity.[23,24] This improvement is attributed to higher thermal energy during calcination, which facilitates the migration of atoms to the correct lattice positions and reduces defect concentrations.[23–25]

XPS was used to evaluate the surface composition and to characterize the chemical and electronic states of the elements present.[26] Fig. 2b–f shows the XPS spectra of $NiFe_2O_4$ nanostructures calcined at 600 °C. The survey spectrum in Fig. 2b confirms the presence of nickel, iron, carbon, and oxygen on the surface. High-resolution spectra for C 1s, Fe 2p, Ni 2p, and O 1s are shown in Fig. 2c–f. A C 1s signal observed in the study is attributed to CO_2 adsorption on the sample surface under

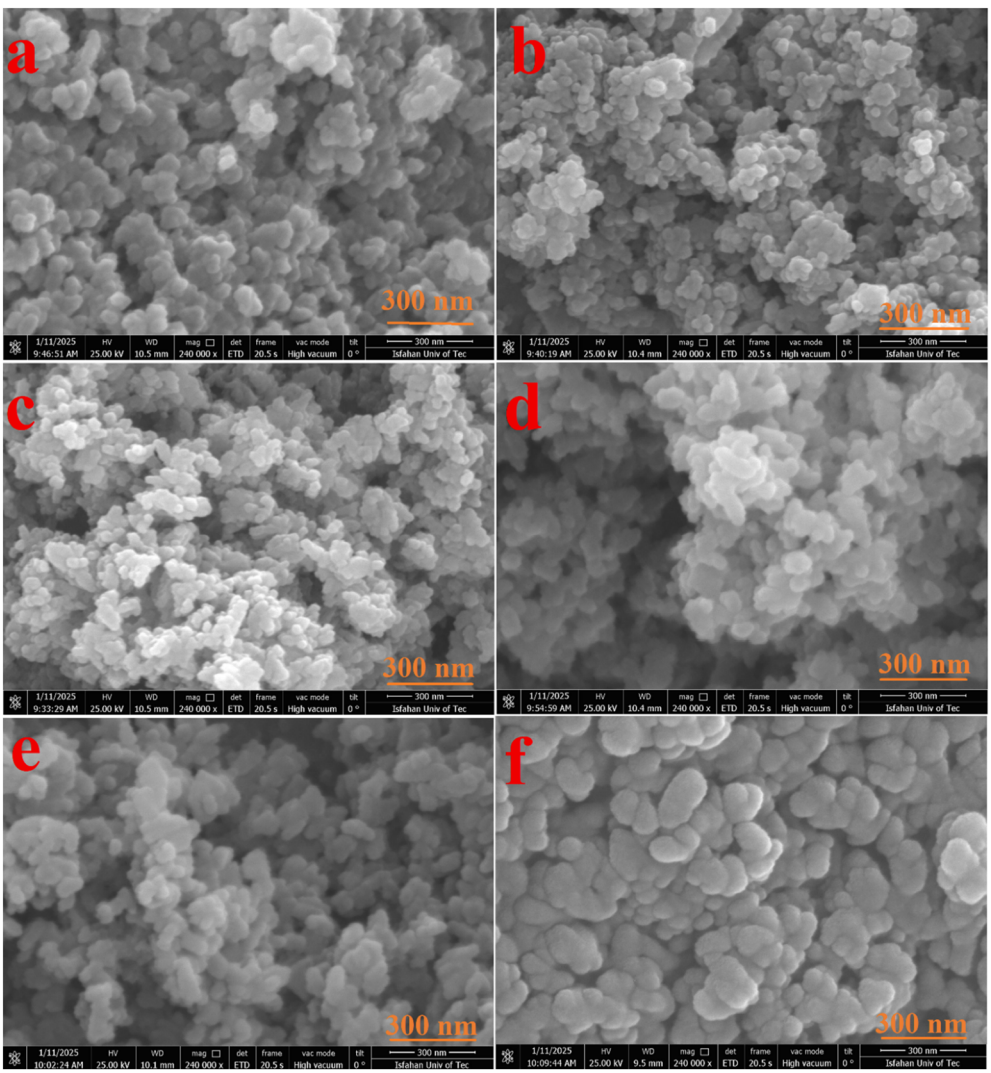

Fig. 3 (a) FESEM images of synthesized $NiFe_2O_4$ nanostructures with the same magnification (240 000 times) (a) NF-400, (b) NF-500, (c) NF-600, (d) NF-700, (e) NF-800, and (f) NF-600 film deposited on the ITO surface.

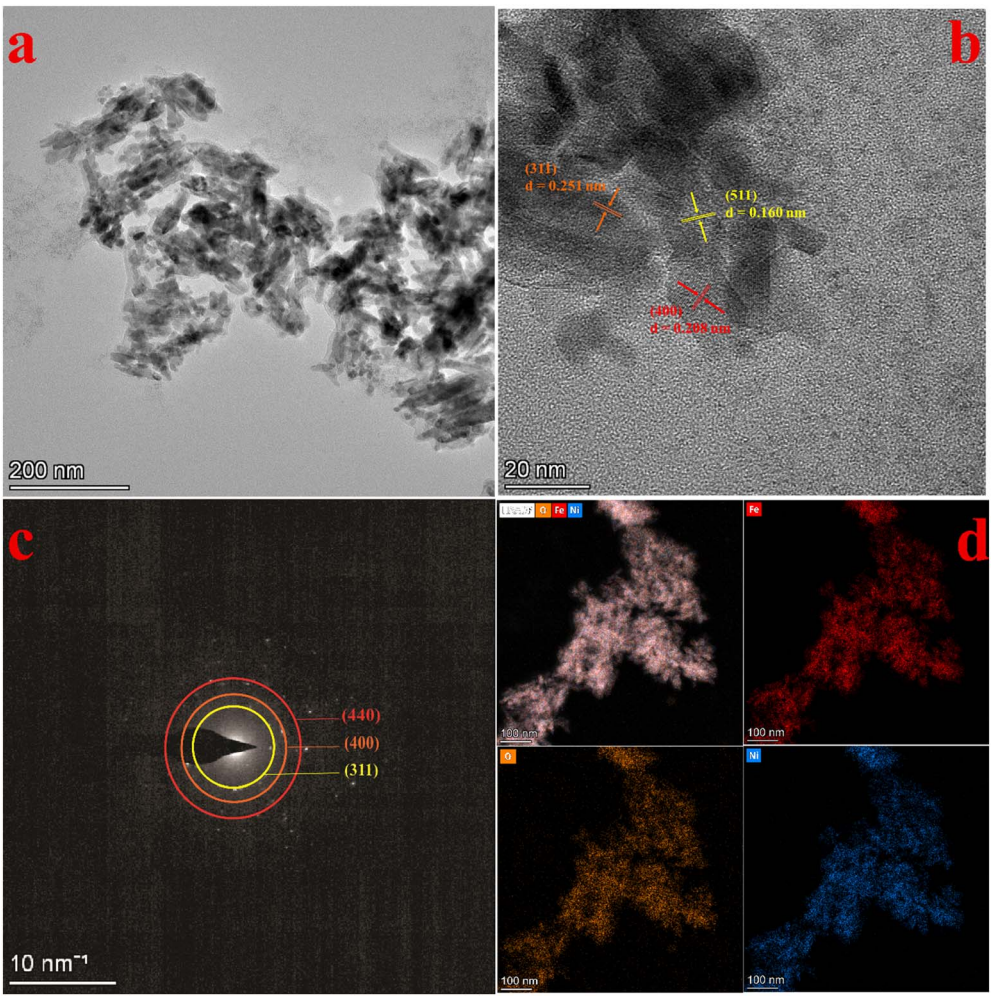

Fig. 4 (a and b) TEM and HRTEM images of $NiFe_2O_4$ nanoparticles (sample NF-600). (c) SAED pattern and (d) TEM element mapping of Fe, Ni, and O.

ambient conditions, a common feature in metal-oxide systems. In the Fe 2p region, two dominant peaks are detected at 711.0 eV (Fe $2p_{3/2}$) and 724.2 eV (Fe $2p_{1/2}$), with shake-up satellites at 718.7 eV and 733.1 eV supporting the presence of Fe^{3+}.[27,28] The Ni 2p region (Fig. 2d) shows four features: Main peaks at 872.2 eV (Ni $2p_{1/2}$) and 854.6 eV (Ni $2p_{3/2}$) and satellite peaks at 878.9 eV and 861.0 eV, indicating the coexistence of Ni^{2+} and Ni^{3+}.[27–30] The O 1s spectrum (Fig. 2c) comprises three components, with a main peak at 529.9 eV corresponding to the lattice oxygen in $NiFe_2O_4$ and weaker contributions at 531.9 eV and 533.4 eV assigned to C–O–C and C–O bonds, respectively.[27–32] The reported binding energies are in agreement with literature values for $NiFe_2O_4$ nanoparticles, confirming the successful material formation.

Both SEM and TEM analyses were conducted to assess the surface morphology and size distribution of the synthesized $NiFe_2O_4$ nanostructures. Fig. 3 shows SEM images of $NiFe_2O_4$ particles produced at different calcination temperatures (also see SI data, Figs. S1–S6). The data indicate that the calcination temperature has only a minor influence on the particle morphology, while the particle size increases from about 40 nm to about 130 nm at higher temperatures. Overall, the particles exhibit a uniform morphology and size distribution, although a certain degree of agglomeration in the synthesized material is unavoidable.[33,34] As the temperature increases, the grain surfaces become increasingly smooth, and the particles become larger, indicating increased agglomeration at higher temperatures and a consequent decrease in the specific surface area of the catalyst. This behavior is consistent with the trends observed in electrochemical measurements. EDX was conducted to determine the surface elemental composition (see SI data, Figs. S7–S11). Elemental mapping of the selected region shows a uniform distribution of Ni, Fe, and O, while the corresponding EDX spectrum further confirms the presence of these elements. These findings are consistent with the results from XRD and XPS analyses (see SI data, Figs. S12–S17).

TEM and HRTEM images of nickel ferrite (sample NF-600) are presented in Fig. 4 (also see SI data, Fig. S18). As shown in Fig. 4a, the $NiFe_2O_4$ particles are uniformly distributed, in good agreement with the SEM results. The HRTEM image (Fig. 4b) displays distinct lattice fringes, confirming the high crystallinity of the synthesized $NiFe_2O_4$. The observed interplanar spacings

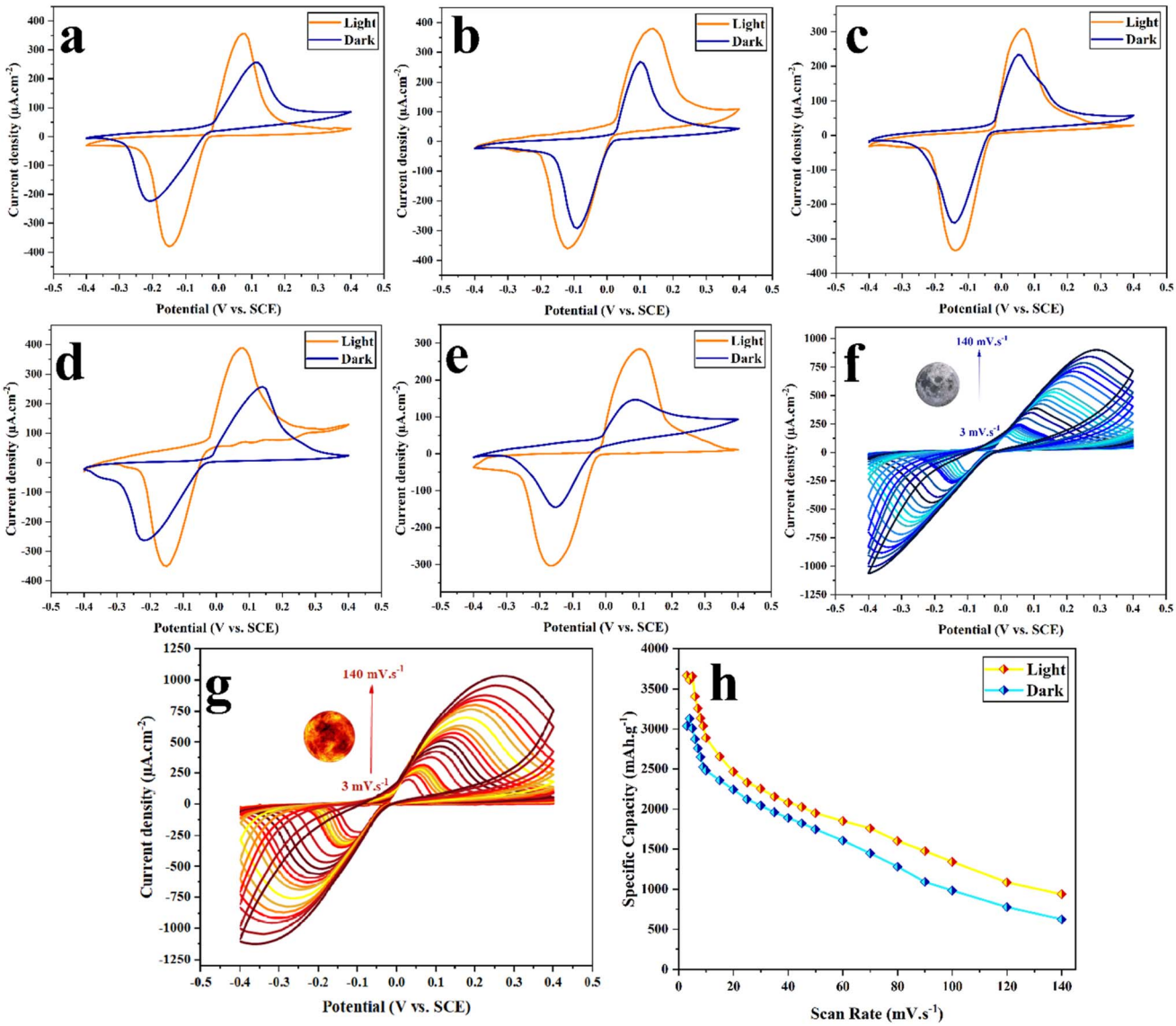

Fig. 5 CV curves comparison of photoelectrodes under dark and illuminated conditions at a scan rate of 9 mV s^{-1}; (a) NF-400, (b) NF-500, (c) NF-600, (d) NF-700, and (e) NF-800. CV curves of the NF-600 sample at different scan rates (f) in the dark and (g) under light illumination. (h) Specific capacitance *vs.* scan rate for the NF-600 sample under light and dark conditions.

of 0.251, 0.160, and 0.208 nm correspond to the (311), (511), and (400) crystallographic planes of the spinel $NiFe_2O_4$ phase, respectively. In addition, the SAED pattern (Fig. 4c) displays distinct rings indexed to the (311), (400), and (440) planes, confirming the material's polycrystalline nature and showing good agreement with the XRD data.[35,36] TEM elemental mapping of $NiFe_2O_4$ (Fig. 4d) reveals a uniform distribution of Fe, Ni, and O throughout the sample.

3.2. Electrochemical and photoelectrochemical evaluation of prepared samples in a three-electrode system

The photoelectrochemical properties of the fabricated photoelectrodes were evaluated using several electrochemical techniques, including CV, GCD, and EIS, in a three-electrode configuration. The tests were performed both in the dark and under illumination. The CV curves for $NiFe_2O_4$/ITO photoelectrodes calcined at different temperatures with and without exposure to light are shown in Fig. 5a–e at a constant scan rate of 9 mV s^{-1}. It can be seen that each cyclic voltammogram exhibits a pair of oxidation and reduction peaks, suggesting that the observed capacitance results largely from pseudocapacitive processes driven by reversible electrochemical reactions involving Ni and Fe. The presence of two prominent redox peaks in each CV curve confirms the pseudocapacitive nature of these materials, which is due to faradaic redox reactions.[37] Comparison of the curves shows that thermal treatment clearly influences the electrochemical properties of the resulting electrodes. At a fixed scan rate, CV areas for all samples under illumination exceed those recorded in the dark, suggesting that light exposure increases their specific capacity. These results show that direct illumination of the photoelectrode increases its specific capacitance and confirm that all

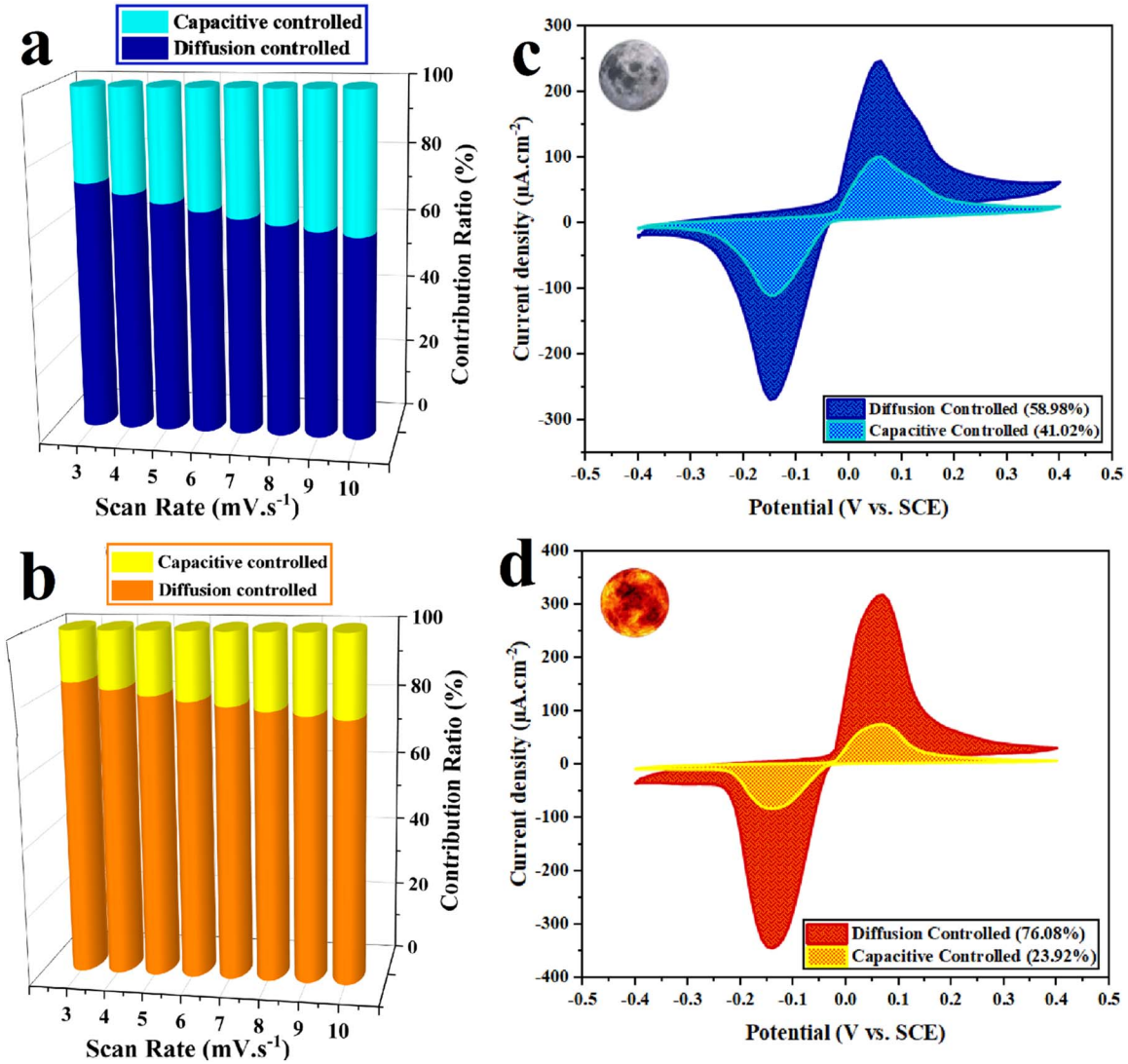

Fig. 6 Charge storage contribution of the NF-600 sample; diffusive and capacitive contribution at different scan rates (a) in the dark and (b) under light illumination. CV curve with diffusion charge storage and capacitive percentage at 10 mV s^{-1} (c) in the dark and (d) under light illumination.

samples exhibit a photo-response with photo-enhanced supercapacitive performance. Fig. 5f and g shows the CV curves for the NF-600 sample recorded at different scan rates. The curves maintain their overall shape with increasing scan rate, suggesting excellent rate capability.[38] As the scan rate increases, the oxidation peak shifts to a more positive potential, while the reduction peak shifts to a more negative potential. At higher scan rates, the CV curves show greater peak spacing, indicating faster interfacial faradaic kinetics and improved electronic and ionic transport, which together contribute to enhanced overall performance.[39] This trend indicates that the material becomes more electrochemically active at higher scan rates, resulting in a larger peak area in the corresponding CV curves. Furthermore, the anodic and cathodic peaks exhibit more symmetrical shapes at higher scan rates, indicating favorable electrochemical properties. Fig. 5h shows the relationship between the scan rate and the specific capacitance (C_{sp}), whereby an inverse correlation can be recognized: C_{sp} decreases with increasing scan rate. At all scan rates, there is consistently a higher capacitance with illumination than in the dark, with the illuminated measurements exceeding those obtained in the dark. In the dark, at a slow scan rate of 3 mV s^{-1}, the capacity is 3037.02 mA h g^{-1}; under illumination, it increases to 3668.19 mA h g^{-1}. At a higher scan rate of 140 mV s^{-1}, the capacity is 624.47 mA h g^{-1} in the dark and 938.86 mA h g^{-1} under illumination. The percentage improvement was calculated using the following equation:

$$\text{Enhancement } (\%) = \left(\frac{C_{\text{light}} - C_{\text{dark}}}{C_{\text{dark}}}\right) \times 100 \quad (1)$$

where C_{light} and C_{dark} denote the specific capacities of the sample under light and dark conditions, respectively. According to the CV data, illumination at a scan rate of 3 mV s^{-1} leads to an increase of 20.78% compared to dark conditions. When the scan rate increases to 140 mV s^{-1}, the improvement increases to 50.34%.

To elucidate the mechanism of charge storage in the electrode, the Dunn method is used to determine whether the total capacity results from a diffusion-driven process ($b = 0.5$), a capacitive contribution from the surface ($b = 1$), or a combination of both.[40] In general, capacitive contributions can be analyzed from CV data using the power-law relationship described below:[41]

$$i = av^b \quad (2)$$

In this context, i denotes the peak current and v denotes the scan rate. The parameters a and b are adjustable. The b-value is obtained from the slope of the plot of $\log(i)$ *versus* $\log(v)$.

$$\log(i) = \log(a) + b\log(v) \quad (3)$$

These equations describe the relationship between peak current (i) and scan rate (v). The slope of the logarithmic plot of i against v is used to determine the b value, which provides information about capacitive or diffuse behavior. A capacitive

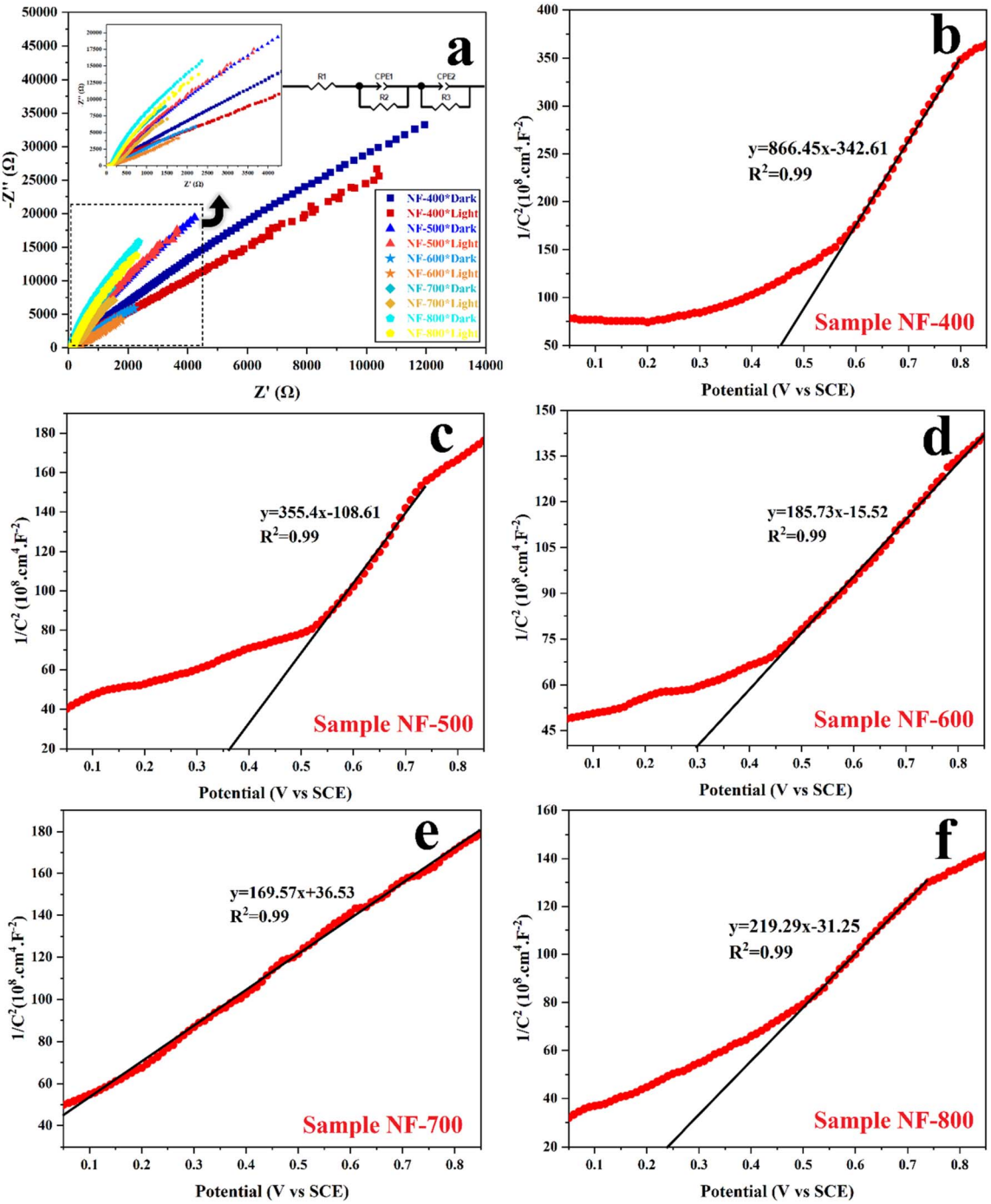

Fig. 7 (a) EIS diagrams of different electrodes in dark and light irradiation. (b–f) Mott–Schottky plots for all five samples.

Table 1 Summary of the results obtained from the Mott–Schottky plots for different $NiFe_2O_4$-based electrodes

Sample	Slope	Intercept	N_D (cm^{-3})	V_{fb} (V)
NF-400	866.45	−342.61	9.31505×10^{17}	0.395418
NF-500	355.4	−108.61	2.27097×10^{18}	0.305599
NF-600	158.73	−15.52	5.08475×10^{18}	0.097776
NF-700	169.57	36.53	4.7597×10^{18}	−0.21543
NF-800	219.29	−31.25	3.68053×10^{18}	0.142505

contribution corresponds to $b = 1$, while a value close to $b = 0.5$ indicates diffusion-controlled behavior.[42–44] The b-values for cathodic and anodic currents are 0.70/0.71 in the dark and 0.65/0.65 under illumination. These results suggest that the charge storage mechanism involves both capacitive and diffusion-driven processes. Under illumination, the capacitive contribution decreases for the anodic current and increases for the cathodic current. In addition, the capacitive contributions include capacitance-controlled reactions ($k_1\nu$) and diffusion-controlled reactions ($k_2\nu^{1/2}$); these can be quantified using the following equation:

$$i(V) = i_{diff} + i_{cap} = k_1\nu + k_2\nu^{1/2} \quad (4)$$

The total current is often expressed as the sum of the capacitance and diffusion-driven contributions. Without light, the capacitance contributions for the NF-600 electrode are 27%, 30%, 32%, 35%, 36%, 38%, 39%, and 41% at scan rates of 3, 4, 5, 6, 7, 8, 9, and 10 mV s^{-1}, respectively (Fig. 6a). The surface capacitance contribution increases with increasing scan rate because, at higher scan rates, the electrolyte ions can react more quickly, especially on the surface, and have less time to diffuse into the interior of the material. Under light, the capacitance contributions are 14%, 16%, 18%, 19%, 20%, 21%, 22%, and 23% at scan rates of 3, 4, 5, 6, 7, 8, 9, and 10 mV s^{-1}, respectively (Fig. 6b).

The capacitance contribution increases with scan rate under illumination. A comparative analysis of Fig. 6(c and d) shows that diffusion-driven contributions dominate over surface capacitance contributions under illumination. When exposed to light, the semiconductor electrodes generate electron–hole pairs. The resulting charge carriers increase overall mobility and provide a stronger driving force for ion intercalation and redox reactions in the bulk, promoting diffusion-controlled processes. Charge carriers generated by light alter the internal chemical potential gradient, effectively increasing the diffusion coefficients for ions within the material. Illumination can also activate or accelerate slow bulk redox (faradaic) reactions in which charge transfer with the electrolyte occurs, resulting in diffusion-limited current contributions as ions migrate to the reaction sites inside. In general, charge carriers generated by

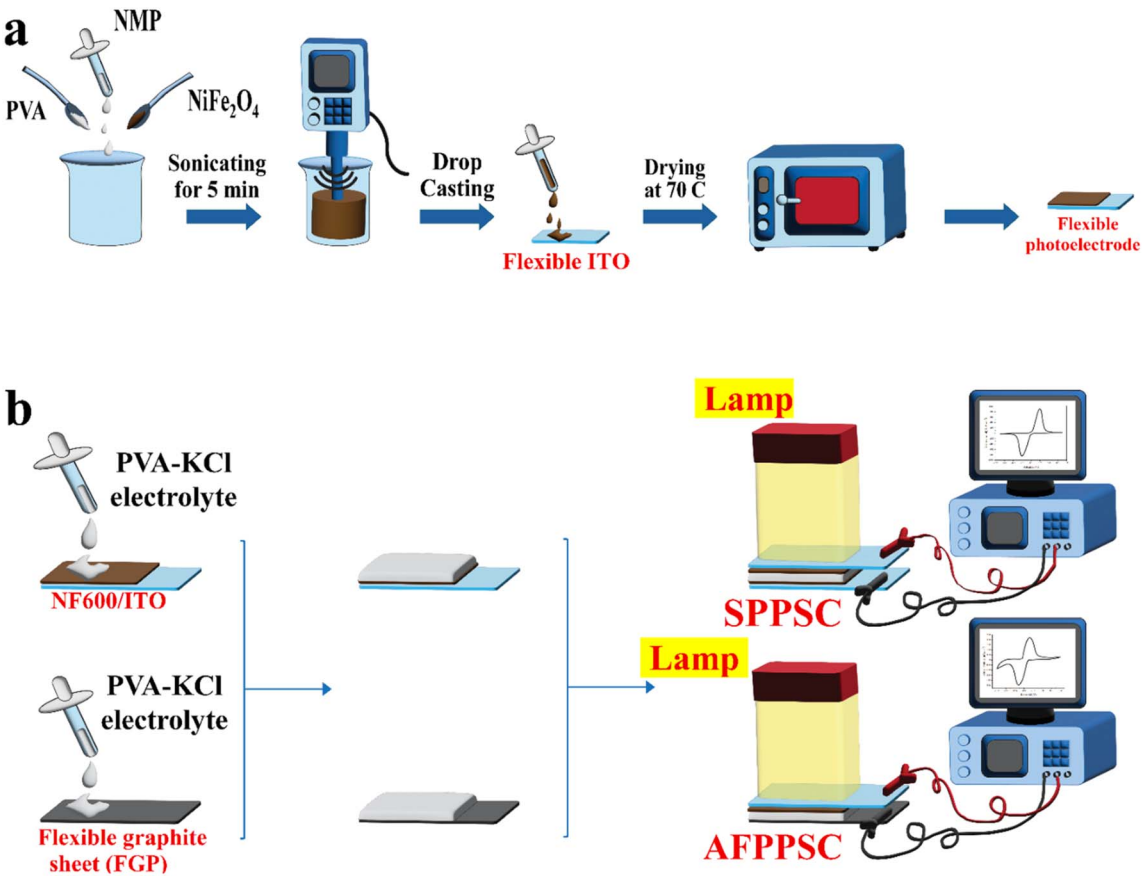

Fig. 8 Schematic of the fabrication process of (a) electrodes and (b) symmetric and asymmetric photo-powered supercapacitors with a sandwich structure.

light enhance diffusion-driven intercalation and redox reactions, shifting storage towards diffusion-dominated behavior and increasing diffusion-limited currents compared to surface capacitive currents.

The GCD curves obtained for the prepared photoelectrodes, under both illuminated and dark conditions, show an extended discharge time when illuminated, indicating a notable enhancement of surface capacitance due to light exposure. Additionally, the NF-600 electrode exhibits a considerably longer discharge time, reflecting a higher capacitance compared with the other samples (see SI data, Fig. S19–S21). The OCP measurements under dark and illuminated conditions provide direct evidence of photo-induced charge separation and the shift in electrode potential upon light exposure. Furthermore, chopped (light/dark) chronoamperometry and chopped LSV confirm the reversible and stable photoresponse, demonstrating enhanced photocurrent generation under periodic illumination. These results collectively verify the photoactivity of the electrode and substantiate its functional role in photo-assisted energy storage within the photo-powered supercapacitor system. Detailed figures and discussions are provided in the SI (see Fig. S22–S24).

EIS analysis can evaluate the internal resistance and capacitive behavior of the photoelectrodes (Fig. 7a). A lower equivalent series resistance indicates improved conductivity of the photoelectrode material under illumination. The Nyquist diagrams display nearly identical impedance slopes in the low-frequency range under both illuminated and dark conditions, suggesting that ion diffusion resistance changes only slightly upon irradiation (see also SI data, Fig. S25). Overall, these observations support the involvement of charge carriers generated by light. Illumination enhances the photoelectrochemical performance of the synthesized photoelectrodes through a synergistic photoelectric effect. In order to better

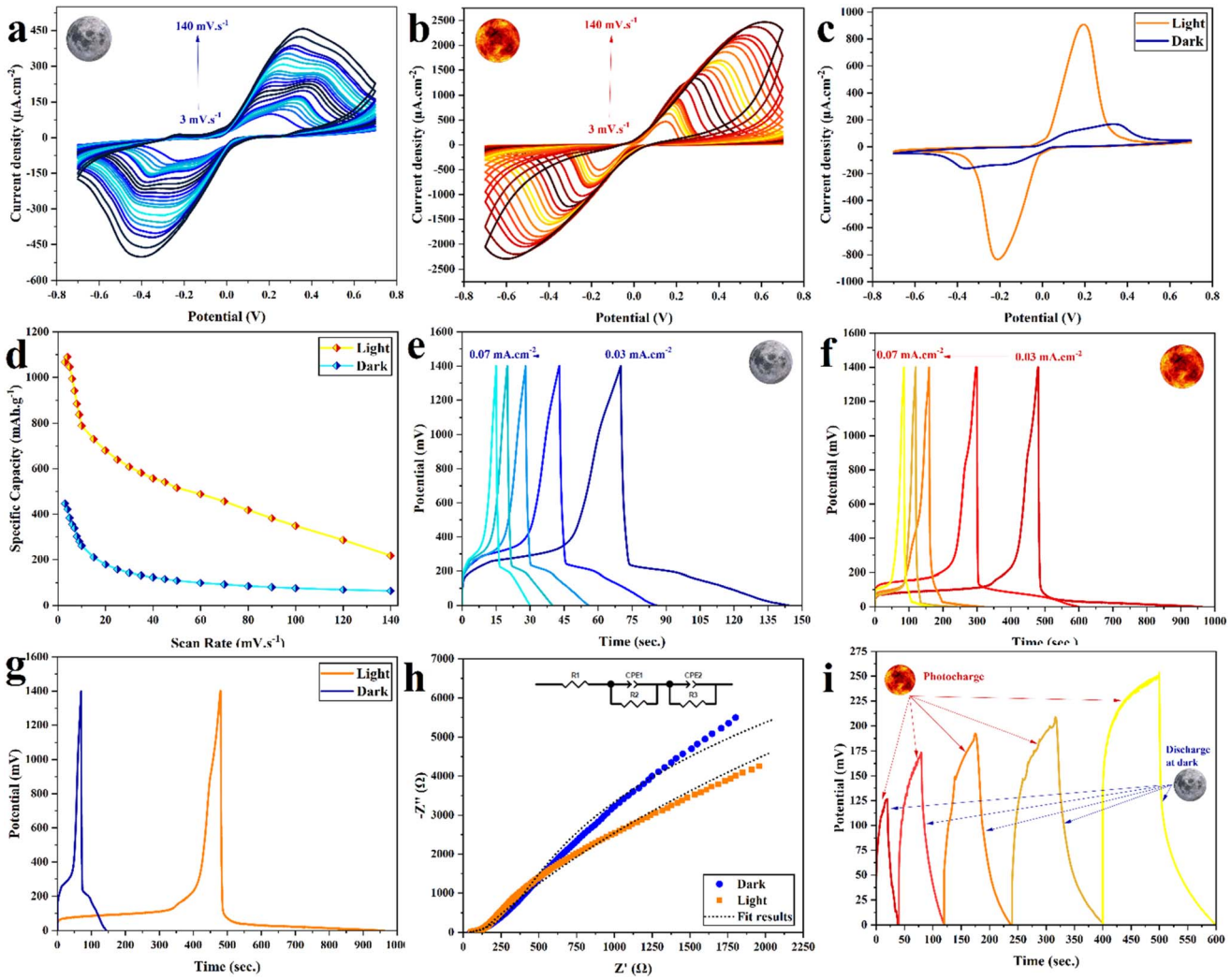

Fig. 9 Electrochemical performance of NF-600//NF-600 symmetric photo-powered supercapacitor (SPPSC); (a) CV curves at various scan rates under (a) dark and (b) light conditions. (c) CV curves at 9 mV s^{-1} of this device with light on or off. (d) Specific capacitance as a function of scanning rate with and without light irradiation. GCD curve at various current densities under (e) dark and (f) light conditions. (g) GCD curves at the current density of 0.03 mA cm^{-2} with light on or off. (h) Nyquist plot of the device with and without light irradiation. (i) Photocharging of this device at various time periods.

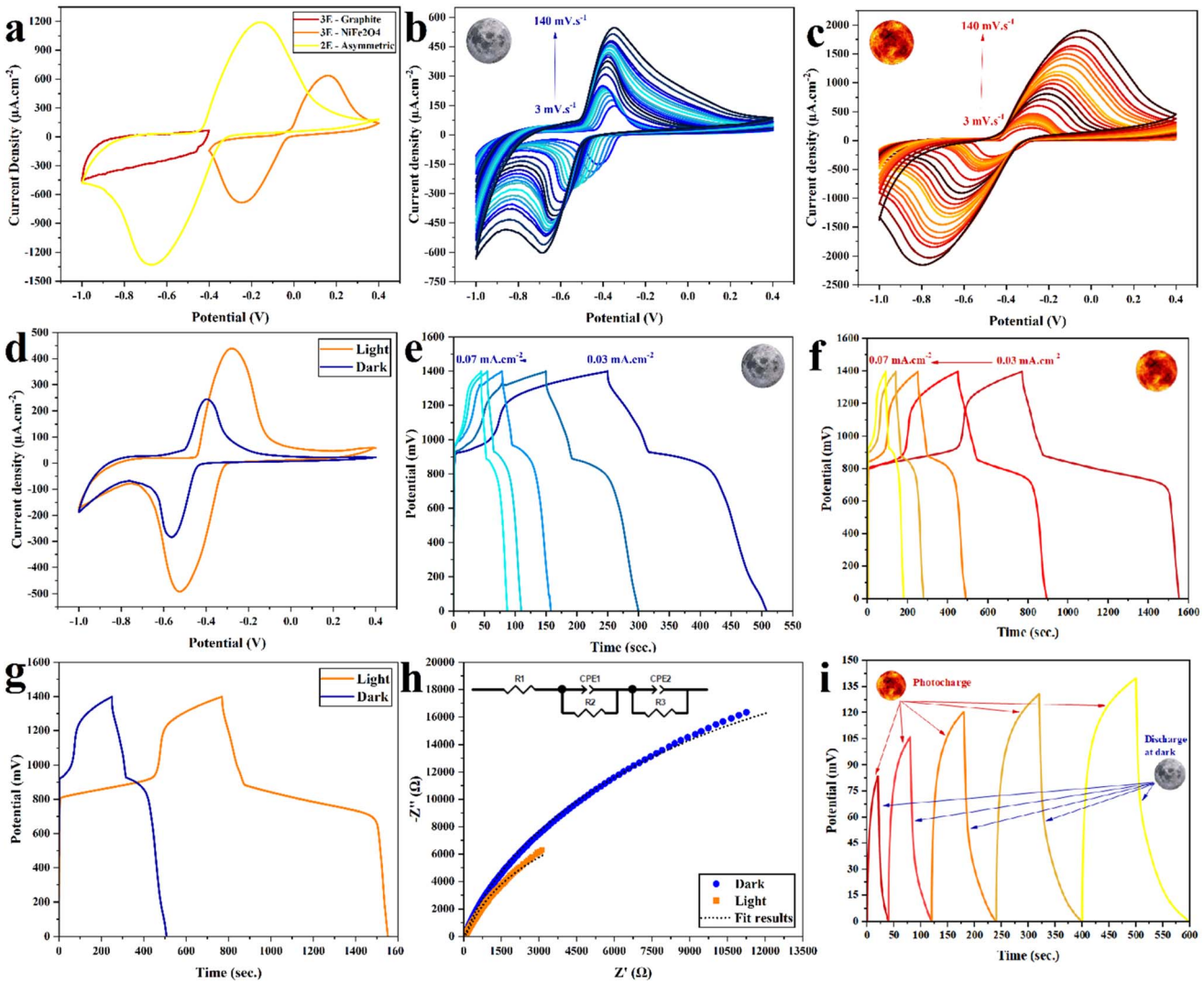

Fig. 10 Electrochemical performance of the asymmetric flexible photo-powered supercapacitor (AFPPSC) with the NF-600//FGP configuration. (a) CV profiles of graphite foil (FGP), and $NiFe_2O_4$ measured in a three-electrode setup. CV curves at various scan rates (3–140 mV s^{-1}) under (b) dark and (c) illuminated conditions. (d) CV curves at a fixed scan rate of 9 mV s^{-1} with the light on and off. GCD curves at a range of current densities (e) in dark and (f) light conditions. (g) GCD curves at 0.03 mA cm^{-2} current density for light-on and light-off scenarios. (h) Nyquist plot of the device with and without light irradiation. (i) Photo charging behavior of device at various time periods.

clarify the impedance analysis, an equivalent electrical circuit (EEC) model was employed to fit the EIS spectra, and the corresponding extracted fitting parameters are summarized in Table S1 (see SI data). Mott–Schottky (M–S) measurements were conducted for all fabricated electrodes to further elucidate their semiconductor properties (Fig. 7b–f, also see SI data, Fig. S26). The linear $1/C^2$–V plots with positive slopes confirm the n-type behavior of the $NiFe_2O_4$-based electrodes. The flat-band potential (E_{fb}) was determined from the x-intercept, and the donor density (N_D) was calculated from the slope of the linear region. Notably, the donor density (N_D) increased as the calcination temperature rose from 400 to 600 °C, indicating enhanced charge carrier concentration and improved photoelectrochemical performance. However, when the temperature was increased beyond 600 °C, the N_D value decreased, suggesting that excessive heat treatment may cause structural changes or defect reduction that adversely affect the charge carrier density. A summary of the electrochemical parameters extracted from the Mott–Schottky plots for the different $NiFe_2O_4$-based electrodes is presented in Table 1.

3.3. Two-electrode measurements

Both symmetric and asymmetric photo-powered supercapacitors (PPSCs) were constructed and tested to assess the practical applicability of the synthesized electrodes. Based on the electrochemical results from the three-electrode studies, NF-600 was used as both the positive and negative electrodes in a symmetric configuration. An asymmetric FPPSC was constructed using NF-600 as one electrode and flexible graphite foil (FGP) as the other. An asymmetric device uses two different electrode materials, allowing for a higher operating voltage and

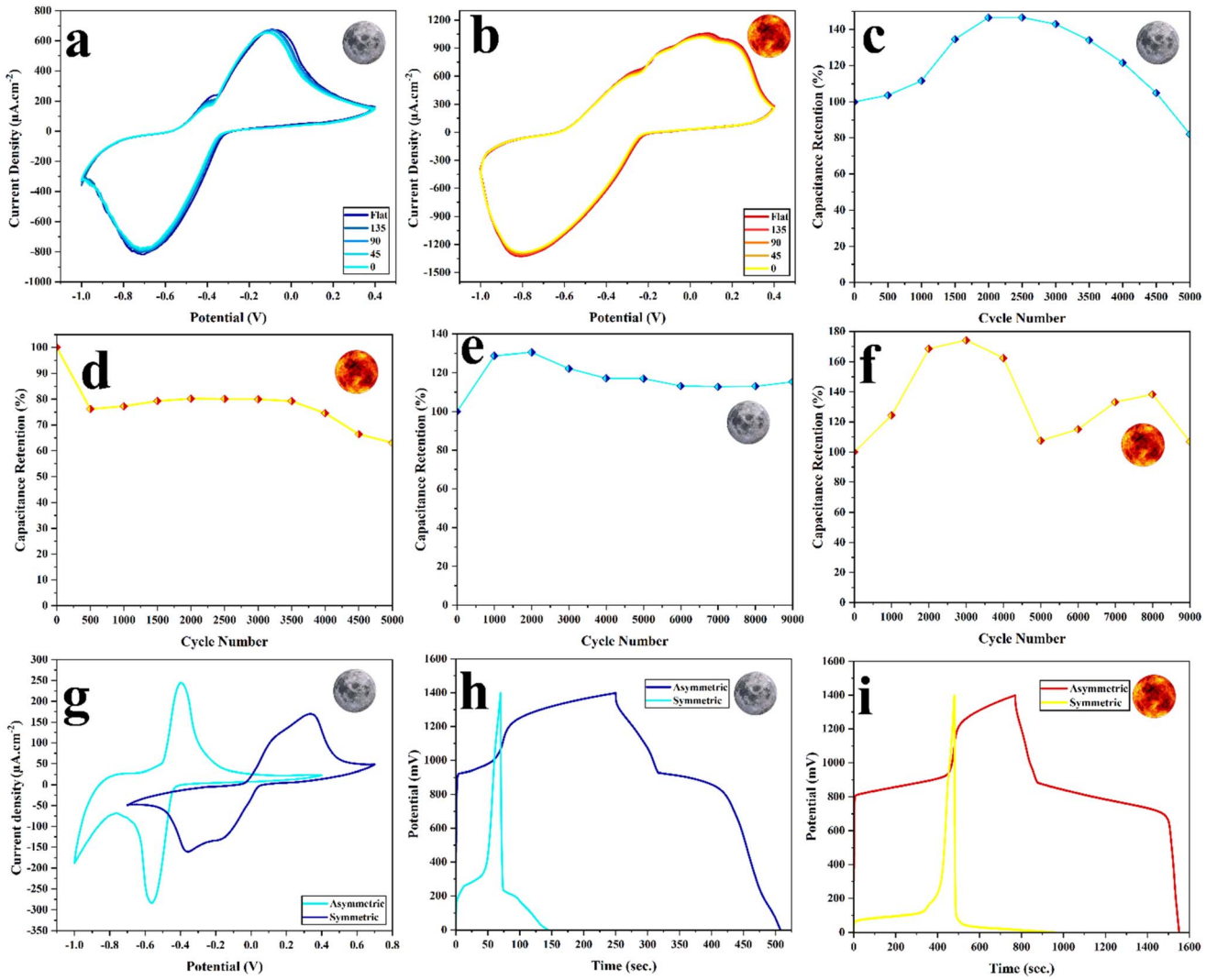

Fig. 11 CV curves of the flexible photo-powered supercapacitor (AFPPSC) at different bending angles under (a) dark and (b) illuminated conditions. Plot of capacitance retention (c) in dark and (d) light conditions. Capacitance retention of the asymmetric photo-powered supercapacitor (e) in dark and (f) light conditions. (g) Comparison of CV responses of symmetric and asymmetric supercapacitors in the dark. Comparison of GCD curves between symmetric and asymmetric supercapacitors (h) in dark and (i) light conditions.

tailored performance.[45] Fig. 8 presents a schematic illustration of the assembled devices.

3.3.1. NF-600//NF-600 symmetric photo-powered supercapacitor (SPPSC). Fig. 9a and b shows the CV curves measured at scan rates from 3 to 140 mV s^{-1}, both without and with light illumination. The CVs were measured over a wide potential range of 1.4 V, showing peak current responses in both the anodic and cathodic directions. As the scan rate increases, the anodic and cathodic peak currents increase, while the spacing between the peaks and the shift in peak positions become more pronounced. Analysis of the CV curves shows that the total enclosed area increases significantly as the scan rate increases from 3 to 140 mV s^{-1}. This increase reflects improved ion transport within the electrolyte between the electrodes, indicating enhanced overall electrochemical activity. At higher scan rates, distinct anodic and cathodic peaks remain identifiable, indicating that reversibility is maintained under these conditions. The CV curves with and without light irradiation at a scan rate of 9 mV s^{-1} are shown in Fig. 9c. The CV curves demonstrate that light irradiation enhances the electrochemical performance of the device. This improvement occurs because excitons generated by light reduce the resistivity of the electrode material, facilitating charge transfer during electrolysis and highlighting the material's favorable electronic properties.[46,47] Under illumination, the peak current increases and the peak potentials shift to lower values. This phenomenon can be attributed to illumination promoting faster charge transfer at the interface by generating electron–hole pairs, which reduces the required overvoltage and shifts the peak potential to lower values. Additionally, light-induced shifts in interfacial energy levels facilitate oxidation and reduction at reduced potentials. Furthermore, illumination alters the adsorption/desorption

dynamics and surface states, contributing to the observed potential shift. Fig. 9d shows the specific capacitance of the device under ON/OFF light conditions. Under illumination, the device demonstrates higher capacitance across all current densities compared with the dark (light-off) condition.

The GCD curves were recorded at different current densities from 0.03 to 0.07 mA cm^{-2} within a high potential window of 1.4 V, both with the light switched off and on (Fig. 9e and f). All GCD curves exhibit distorted triangular shapes, with voltage plateaus observed in both the charging and discharging regions. These plateaus indicate that redox reactions occur during the charge and discharge processes. The specific capacities of this device in the dark are 19.01, 14.73, 12.79, 11.46, and 9.62 mA h g^{-1} in the range of 0.03–0.07 mA cm^{-2}, indicating that the specific capacity of this device decreases with increasing current density under both conditions. This decrease is likely caused by the limited electrolyte volume and high current density, which impedes ion diffusion and migration across the electrodes.[48] It was also found that the charge–discharge time for this device was longer under light than in the dark (Fig. 9g). Under illumination, the storage capacity increases due to the generation of photogenerated charges that enter the external circuit, improving charge transport and the device's capacity. Simultaneously, the holes generated by light participate in oxidation, promoting higher valence states and accelerating redox reactions. Additionally, holes photogenerated during the charging process drive oxidation, facilitating ion transitions to higher valence states and further accelerating the redox reaction. The Nyquist plots for the assembled devices (Fig. 9h) show small semicircles accompanied by vertical lines, indicating rapid charge transfer and excellent capacitive behavior, respectively (see also SI data, Table S2).[47] To demonstrate the self-charging properties of the assembled SPPSC device, it was charged for different durations under illumination without bias voltage, and the photovoltage was measured (Fig. 9i). Increasing the irradiation time from 20 s to 100 s raises the photovoltage of the device from 125 mV to 250 mV, indicating improved photoelectrochemical performance and energy storage capability under illumination.

3.3.2. NF-600//FGP asymmetric flexible photo-powered supercapacitor (AFPPSC). In a three-electrode configuration, the $NiFe_2O_4$/ITO electrode exhibits a working potential window of −0.4 to 0.4 V, while the flexible graphite foil (FGP) displays a window of −1.0 to −0.4 V at a scan rate of 50 mV s^{-1} (Fig. 10a). The CV profiles indicate pseudo-capacitive behavior for $NiFe_2O_4$ and electrical double layer capacitance (EDLC) for GP.[49] Using the individual electrode potentials determined in the three-electrode configuration, the operating cell voltage for the fabricated asymmetric NF6-00//FGP device was optimized to 1.4 V (Fig. 10a). CV measurements of the AFPPSC device were conducted at scan rates from 3 to 140 mV s^{-1} under a fixed bias voltage of 1.4 V, both in the dark and under light irradiation (Fig. 10b and c). Increasing the scan rate results in higher current responses and a larger area under the CV curves, indicating rapid ion transport in the electrolyte (see also SI data, Fig. S27). Notably, the CV profiles remain consistent as the scan rate increases from 3 to 140 mV s^{-1}.

The GCD evaluation for the NF-600//FGP device was carried out over a potential window from 0 to 1.4 V at various current densities (see also SI data, Fig. S28). The nonlinear GCD profiles demonstrate the interaction between $NiFe_2O_4$ and GP, reflecting a combined contribution of pseudocapacitance and EDLC mechanisms. Furthermore, the GCD curves maintain their overall shape across different current densities under illumination, indicating that the electrodes retain robust performance when exposed to light (Fig. 10e and f). A minimal voltage drop is observed in the GCD profiles, indicating favorable electrochemical behavior and good reversibility of the device. Compared with the photo-powered supercapacitor's performance under dark conditions, illumination results in an expanded CV area and longer charge–discharge durations (Fig. 10d and g). At current densities of 0.03, 0.04, 0.05, 0.06, and 0.07 mA cm^{-2}, the specific capacitances under light are 1.58, 1.21, 0.77, 0.53, and 0.39 mA h cm^{-2} (390.1, 299.3, 191.3, 130.7, and 96.8 mA h g^{-1}), respectively. In comparison, the corresponding values in the absence of light are 0.47, 0.39, 0.24, 0.2, and 0.19 mA h cm^{-2} (117.1, 95.9, 61.1, 50.99, and 47.1 mA h g^{-1}). These results indicate a substantial improvement of the energy storage capability of the AFPPSC device upon light exposure.[50]

EIS measurements were conducted on the AFPPSC device under both dark and illuminated conditions to evaluate the effect of light on its performance (Fig. 10h). The Nyquist plots display similar shapes under both conditions in the high and low frequency regions. Under illumination, the charge-transfer resistance decreases significantly, while the capacitance increases, indicating marked photo responsive behavior. This suggests that photoexcitation promotes electron transfer across the interfaces and enhances charge storage at the electrode surfaces, resulting in a higher specific capacitance than in the dark state (see also SI data, Table S2).

We conducted photo charging-galvanostatic discharge (PC-GD) tests on the AFPPSC at various photo charging durations,

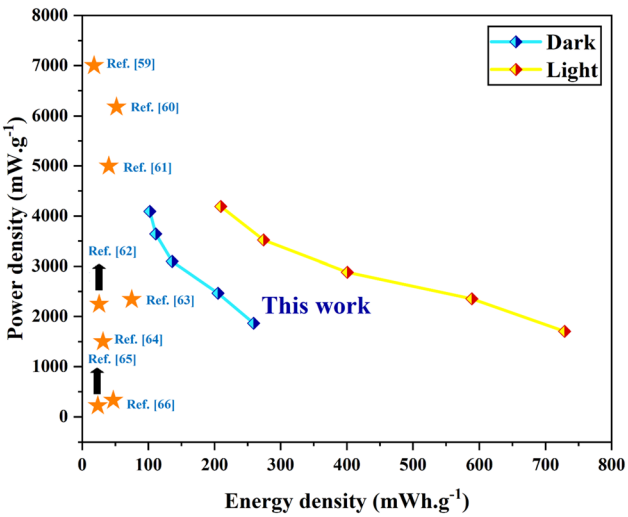

Fig. 12 Comparative Ragone plot illustrating the relationship between specific energy density (mWh g^{-1}) and power density (mW g^{-1}) for all $NiFe_2O_4$-based supercapacitor electrodes.

Table 2 Comparison of the electrochemical energy storage parameters of $NiFe_2O_4$-based supercapacitors in this study with those reported in the literature

Materials	Synthesis method	Potential window (V)	Electrolyte	Specific capacitance ($F\ g^{-1}$)	Current density	Retention (cycles)	Energy density ($Wh\ kg^{-1}$)	Power density ($W\ kg^{-1}$)	Ref.
$NiFe_2O_4$/rGO	Microwave	0–0.5	6 M KOH	1320	1 A g^{-1}	94% (5000)	75	2343	63
$NiFe_2O_4$	Chemical bath deposition	0–1.2	6 M KOH	236	0.3 A g^{-1}	98% (7000)	47	333	66
$NiFe_2O_4$@CC	Hydrothermal	0–1	1 M H_2SO_4	1135.5	1.29 A g^{-1}	82.4% (2400)	2.07 mWh cm^{-2}	—	67
$NiFe_2O_4$	Co-precipitation	0–0.5	6 M KOH	398	1 A g^{-1}	98% (6500)	27.71	14 490	68
$NiFe_2O_4$	Electrodeposition	−0.8–0.2	1 M KOH	560	1 A g^{-1}	95.3% (10 000)	40.3	5000	61
$NiFe_2O_4$/MOF	Solvothermal	−0.1–0.5	1 M KOH	833	0.25 A g^{-1}	74% (3000)	42	154	69
$NiFe_2O_4$@$NiFe_2O_4$	Hydrothermal	−0.2–0.8	2 M KOH	1451.5	5 mA cm^{-2}	95.3% (3000)	33.6	367.3	70
NiO/$NiFe_2O_4$	Hydrothermal	0–0.5	2 M KOH	248.4	1 A g^{-1}	89.2% (2000)	—	—	71
$NiFe_2O_4$/NFO	Hydrothermal	−0.2–0.4	3 M KOH	560	15 A g^{-1}	—	—	—	72
$NiFe_2O_4$/ carbon nanofibrous	Electrospining	0–1	1 M H_2SO_4	343	0.2 A g^{-1}	97.4% (10 000)	31.6	1500	64
$NiFe_2O_4$/rGO	Hydrothermal	−1.1–−0.2	1 M Na_2SO_4	210.9	0.5 A g^{-1}	94.2% (5000)	23.7	225	65
$NiFe_2O_4$/rGO	Hydrothermal	−1.2–−0.2	1 M Na_2SO_4	345	1 A g^{-1}	60% (500)	—	—	73
$NiFe_2O_4$/rGO	Chemical vapor deposition	0–0.4	2 M KOH	1028	2 A g^{-1}	94% (10 000)	18	7000	59
$NiFe_2O_4$/rGO	Hydrothermal	0–1.1	1 M $LiClO_4$	1090	0.5 A g^{-1}	94% (750)	660	2500	74
$NiFe_2O_4$/rGO	Hydrothermal	0–0.5	1 M KOH	584	10 mV s^{-1}	91% (2000)	—	—	75
$NiFe_2O_4$/graphene	Hydrothermal	−1–0	6 M KOH	481.3	0.1 A g^{-1}	99% (10 000)	—	—	76
$NiFe_2O_4$/graphene	Hydrothermal	0–0.45	6 M KOH	464.15	1 A g^{-1}	140%. (5000)	—	—	77
$NiFe_2O_4$/CNT	Hydrothermal	−0.1–0.5	2 M KOH	1291	1 A g^{-1}	81% (500)	23	872	78
$NiFe_2O_4$/alloy-graphene	Thermal liquid fusion	0–0.5	3 M KOH	845	1 A g^{-1}	94.3% (5000)	30.8	620	13
$NiFe_2O_4$@graphene	Solution based process	0–1	1 M Na_2SO_4	207	0.5 mA	95% (1000)	—	—	79
PANI-$NiFe_2O_4$	Combustion	−0.2–1	1 M H_2SO_4	448	1 mA cm^{-1}	80% (1000)	25.7	2249	62
$NiFe_2O_4$/MoS_2	Hydrothermal	0–0.6	1 M KOH	506	1 A g^{-1}	90.7% (3000)	—	—	80
$NiFe_2O_4$/polypyrrole	Sol–gel auto combustion	−1.2–0.4	1 M H_2SO_4	721.66	1 A g^{-1}	99.08% (1000)	51.95	6180	60
$NiFe_2O_4$	Co-precipitation	−0.4–0.4	2 M KCl	390.15 mA h g^{-1} (light) 117.13 mA h g^{-1} (dark)	0.03 mA cm^{-2}	115% (light) 106% (dark) (9000)	729.12 (light) 259.20 (dark)	1704.45 (light) 1866.29 (dark)	This work

as shown in Fig. 10i. Charging was performed under light irradiation, with no external voltage or current applied. The device was photo charged for 20 s to reach approximately 83 mV, after which discharging was carried out in the dark. The photovoltage increases gradually as the light exposure time increases, and the corresponding discharging time extends accordingly. These results indicate that the assembled devices are highly photo-responsive and function effectively as photo-powered supercapacitors, delivering notable specific capacitance and retaining stored energy after solar charging.

To demonstrate the AFPPSC's mechanical flexibility, the device undergoes CV assessments in its flat (original) configuration and under bent conditions. Fig. 11(a) and (b) present the CV curves for different bending states, in dark and light irradiation conditions, respectively. These curves do not show noticeable distortions in either the flat or bent states, indicating that the device maintains excellent mechanical performance and flexibility.

Cycle performance is essential for evaluating electrochemical supercapacitor devices. The cycling stability of both symmetric and asymmetric configurations was assessed by galvanostatic charge–discharge cycling at a current density of 0.12 mA cm^{-2} under both light and dark conditions, as shown in Fig. 11(c–f). For the symmetric devices, the initial specific capacitance retained after 5000 cycles was approximately 82% in the dark and 63% under illumination, both lower than that observed for the asymmetric cell. When illuminated, the symmetric cell showed an initial decline to about 76.2% of its starting capacitance after 500 cycles, after which the loss rate slowed, stabilizing around 63% after 5000 cycles. Under dark conditions, the capacitance initially increased, followed by a decline after approximately 2500 cycles. In contrast, the asymmetric cell exhibits distinct behavior. Rather than fading, its capacitance progressively increases with continued cycling. The asymmetric supercapacitor reaches 115% and 106% of its initial capacitance after 9000 cycles under dark and illuminated conditions, respectively, which is attributed to an activation process occurring during cycling tests. This gradual activation is thought to result from deeper electrolyte ion penetration into the interior regions of the electrode, enhancing charge storage during extended operation.[51–58]

Fig. 11g–i compares the electrochemical performance of asymmetric and symmetric cells. Analysis of the CV curves shows that the asymmetric cell has a larger overall loop area than the symmetric supercapacitor, indicating enhanced capacitive performance. Therefore, the asymmetric configuration is expected to deliver higher capacitance than its symmetric counterpart. The asymmetric cell demonstrates a specific capacitance of 1603.98 mA h g^{-1} at a scan rate of 3 mV s^{-1}, exceeding the symmetric cell's 1067.23 mA h g^{-1}. GCD results obtained under both dark and illuminated conditions were used to evaluate the performance of the supercapacitors, as shown in Fig. 11h and i. Longer charging and discharging durations correspond to higher specific charge capacitance for the device. At an applied current density of 0.03 mA cm^{-2}, the asymmetric supercapacitor exhibits superior performance compared with the symmetric counterpart, as indicated by the extended discharge time in this figure. The GCD curves for both symmetric and asymmetric cells display an ohmic (*IR*) drop, with the drop being more pronounced in the symmetric device. This larger *IR* drop can adversely affect charging and discharging efficiency in the symmetric configuration. In general, asymmetric cells offer advantages over symmetric cells, including higher energy density and power density in supercapacitors, because two distinct electrode materials can be optimized for complementary functions.

The energy and power densities of the fabricated light-driven supercapacitor were systematically evaluated using a Ragone plot (Fig. 12). The results show that, under illumination, the device achieves a maximum energy density of 729.1 mWh g^{-1} at a power density of 1704.4 mW g^{-1}, which is significantly higher than the value obtained under dark conditions (259.2 mWh g^{-1}). This substantial enhancement highlights the important contribution of photo-induced charge carriers to the overall charge storage process. Furthermore, comparison with previously reported $NiFe_2O_4$-based supercapacitor systems (Table 2) shows that the present device exhibits competitive, and in several cases superior, electrochemical performance. These findings further confirm the effectiveness of the photo-enhanced charge storage mechanism in the proposed system.

4. Conclusions

In this study, $NiFe_2O_4$/ITO electrodes were investigated for light-assisted energy storage. $NiFe_2O_4$ nanostructures were synthesized *via* co-precipitation and calcined at 400–800 °C, revealing that calcination strongly affects structural, morphological, and photoelectrochemical properties. The sample calcined at 600 °C exhibited the highest capacitance due to an optimal balance between crystallinity and accessible surface area. Under illumination, all electrodes showed enhanced capacitance, with the NF-600 electrode improving by approximately 21% (CV) and 34% (GCD). Symmetric (NF-600//NF-600) and asymmetric (NF-600//FGP) photo-powered supercapacitors were fabricated, with the asymmetric device achieving a high energy density of 729.12 mWh g^{-1}, a power density of 1704.45 mW g^{-1}, and excellent cycle stability (106% retention after 9000 cycles). Both devices generated self-sustaining voltage under light, demonstrating the potential of $NiFe_2O_4$-based photoactive electrodes for efficient solar-driven energy storage applications.

Author contributions

Shekoufeh Pira: writing – original draft, validation, investigation, formal analysis. Mohamad Mohsen Momeni: writing – review & editing, supervision, resources, methodology, investigation, funding acquisition, conceptualization. Fuxiang Zhang: writing – review & editing, visualization, conceptualization.

Conflicts of interest

The authors declare no conflict of interest.

Data availability

The data that support the findings of this study are available from the corresponding author upon reasonable request.

Supplementary information (SI): additional characterization data (Fig. S1–S18), photoelectrochemical results, and comprehensive three-electrode tests comparing all samples and evaluating the optimal electrode (Fig. S19–S26), as well as supplemental performance data for the assembled devices (Fig. S27 and S28). It also contains two tables comparing relevant literature. See DOI: https://doi.org/10.1039/d5ta10294d.

Acknowledgements

The authors gratefully acknowledge the Research Affairs Division of Isfahan University of Technology (IUT) for partial financial support. This work was also supported by the CAS President's International Fellowship Initiative (PIFI) under Grant No. 2025PVB0071.

References

1 H. Rezk, H. Alhumade, M. Mahmoud, E. T. Sayed, M. A. Abdelkareem and A. Olabi, *Sustain. Horiz.*, 2025, **16**, 100162.
2 A. Anastasovski, Is renewable energy storage sustainable? A review, *Green Technol. Sustainability*, 2025, **3**, 100176.
3 Z. Hosseini, M. M. Momeni, B. K. Lee and A. W. Maijenburg, *Chem. Eng. J.*, 2025, **515**, 163566.
4 A. Bibi, M. Mustaqeem, M. A. Gondal, A. Majeed, P. T. Chou, Y. F. Chen, Z. G. Gu, M. Waqas and A. Ali, *J. Energy Storage*, 2025, **123**, 116696.
5 M. Najafi and M. M. Momeni, *Chem. Eng. J.*, 2025, **507**, 160555.
6 V. A. Savekar, A. M. Teli, S. A. Beknalkar, V. V. Satale, S. S. More and T. S. Bhat, *J. Energy Storage*, 2025, **111**, 115366.
7 P. Sen and A. De, *Electrochim. Acta*, 2010, **55**, 4677–4684.
8 S. Anwar, K. S. Muthu, V. Ganesh and N. Lakshminarasimhan, *J. Electrochem. Soc.*, 2011, **158**, A976–A981.
9 C. Yuan, H. B. Wu, Y. Xie and X. W. Lou, *Angew. Chem., Int. Ed.*, 2014, **53**, 1488–1504.
10 L. X. Shen, L. H. Du, S. Z. Tan, Z. G. Zang, C. X. Zhao and W. J. Mai, *Chem. Commun.*, 2016, **52**, 6296–6299.
11 P. Xiong, J. Zhu and X. Wang, *J. Power Sources*, 2015, **294**, 31–50.
12 Y. Zhao, M. Yuan, Y. Chen, J. Yan, L. Xu, Y. P. Huang, J. B. Lian, J. Bao, J. X. Qiu, L. Xu, Y. G. Xu, H. Xu and H. M. Li, *Electrochim. Acta*, 2018, **260**, 439–448.
13 M. A. Deyaba, A. E. Awadallaha, H. A. Ahmeda and Q. Mohsen, *J. Energy Storage*, 2022, **46**, 103926.
14 I. Hasan, M. Al-hedrewy, M. Al-Bahrani, P. Kanjariya, A. Rajiv, A. Shankhyan, H. M. Albert and D. N. Thatoi, *Diamond Relat. Mater.*, 2025, **153**, 112096.
15 Y. Zhang, Y. Y. Zhang, C. Li, X. H. Yan, S. Hu, R. B. Yin, Y. F. Wei, K. Z. Gao and H. L. Gao, *Coord. Chem. Rev.*, 2024, **519**, 216103.
16 N. K. Lee and W. Y. Sohn, *ChemPhotoChem*, 2024, **8**, e202300301.
17 K. Derkaoui, I. Belkhettab, I. Bencherifa, A. Elfiad, Y. Mebdoua, K. Boukhouidem, S. Benredouane, S. Naama, T. Hadjersi and M. Kechouane, *React. Kinet., Mech. Catal.*, 2025, **138**, 2387–2405.
18 A. Lassoued, M. S. Lassoued, B. Dkhil, S. Ammar and A. Gadri, *J. Mater. Sci.: Mater. Electron.*, 2018, **29**, 7057–7067.
19 Z. Bazhan, F. E. Ghodsi and J. Mazloom, *Appl. Phys. A*, 2016, **122**, 551.
20 R. Kumara, R. Kumarb, P. K. Sahooc, M. Singha and A. Soam, *Mater. Today: Proc.*, 2022, **67**, 1001–1004.
21 N. Sharma, S. Verma, A. Singh, M. Gupta and S. Arya, *Appl. Phys. A*, 2023, **129**, 457.
22 D. Chu, F. Li, X. Song, H. Ma, L. Tan, H. Pang, X. Wang, D. Guo and B. Xiao, *J. Colloid Interface Sci.*, 2020, **568**, 130–138.
23 J. L. Tian, H. Y. Zhang, G. G. Wang, X. Z. Wang, R. Sun, L. Jin and J. C. Han, *Superlattices Microstruct.*, 2015, **83**, 719–729.
24 A. N. Mallika, A. R. Reddy and K. V. Reddy, *J. Adv. Ceram.*, 2015, **4**, 123–129.
25 V. Sharma, J. K. Sharma, V. Kansay, V. D. Sharma, A. Sharma, S. Kumar, A. K. Sharma and M. K. Bera, *Chem. Phys. Impact*, 2023, **6**, 100196.
26 K. O. Otun, S. Zong, D. Hildebrandt and X. Liu, *J. Phys. Chem. Solids*, 2022, **167**, 110779.
27 Z. Li, F. Si, Y. Ma, J. Geng, G. Wang, Z. Wang, R. Yu, J. Mu, J. Hou, Y. Wang, Z. Zhang, H. Che, P. Li and D. Li, *J. Magn. Magn. Mater.*, 2023, **571**, 170589.
28 T. Yamashita and P. Hayes, *Appl. Surf. Sci.*, 2008, **254**, 2441–2449.
29 K. Egizbek, A. L. Kozlovskiy, K. Ludzik, M. V. Zdorovets, I. V. Korolkov, B. Marciniak, M. Jazdzewska, D. Chudoba, A. Nazarova and R. Kontek, *Ceram. Int.*, 2020, **46**, 16548–16555.
30 J. Zhang, Y. Jiang, Y. Wang, C. Yu, J. Cui, J. Wu, X. Shu, Y. Qin, J. Sun, J. Yan, H. Zheng, Y. Zhang and Y. Wu, *Electrochim. Acta*, 2019, **321**, 134652.
31 H. Ahankar, A. Ramazani and S. W. Joo, *Res. Chem. Intermed.*, 2016, **42**, 2487–2500.
32 R. P. Patil, S. B. Teli, V. D. Jadhav, P. D. Kamble and K. M. Garadkar, *J. Mater. Sci.: Mater. Electron.*, 2024, **35**, 84.
33 L. Li, T. Fang, A. Huang, C. Liu, L. Fu, Y. Chen, Y. Ding, N. Mitsuzaki and Z. Chen, *J. Photochem. Photobiol.*, 2023, **445**, 114938.
34 S. N. Jirankalagi, A. C. Molane, S. M. Sutar, R. N. Mulik, M. Selvaraj, K. R. P. Sunajadevi and V. B. Patil, *Synth. Met.*, 2025, **311**, 117836.
35 Z. Fang, Z. Hao, Q. Dong and Y. Cui, *J. Nanopart. Res.*, 2018, **20**, 106.
36 X. Zhao, Y. L. Zhang, X. X. Wang, H. L. Shi, W. Z. Wang and M. S. Cao, *J. Mater. Sci.: Mater. Electron.*, 2016, **27**, 11518–11523.
37 K. Ajravat, O. P. Pandey and L. K. Brar, *J. Power Sources*, 2025, **649**, 237472.
38 X. Chen, X. Chen, F. Zhang, Z. Yang and S. Huang, *J. Power Sources*, 2013, **243**, 555–561.

39 S. Chen, G. Yang, Y. Jia and H. Zheng, *ChemElectroChem*, 2016, **3**, 1490–1496.
40 M. Najafi, M. M. Momeni and B. K. Lee, *Chem. Eng. J.*, 2024, **493**, 152423.
41 K. J. Samdani, D. W. Joh and K. T. Lee, *J. Alloys Compd.*, 2018, **748**, 134–144.
42 P. Wang, G. Zhang, W. Chen, B. Yang, X. Wang, Q. Chen, L. Liu, H. Jiao, X. Deng, L. Yang, W. Zhu and H. Liu, *Colloids Surf., A*, 2024, **682**, 132861.
43 S. Zhang, Y. Liu, H. Wang, X. Sun, M. Li, C. Qin, Z. Wang and H. Sun, *Appl. Surf. Sci.*, 2025, **698**, 163113.
44 K. Xue, L. Tian, X. Zheng, J. Ding, M. Ali, S. Xiao, M. Song and S. Kumar, *Mater. Chem. Phys.*, 2024, **313**, 128712.
45 F. N. M. Souri, R. T. Kumar, D. S. Priya, T. Ali and M. Shkir, *Relat. Mater.*, 2025, **159**, 112900.
46 A. M. Teli, S. A. Beknalkar, V. V. Satale, P. J. Morankar, M. A. Yewale and J. C. Shin, *Surf. Interfaces*, 2023, **40**, 103149.
47 H. Cai, Y. Li, D. Liu, X. Yang, D. Zhou, E. Han, X. Li, Q. Li and Y. He, *Colloids Surf., A*, 2024, **703**, 135386.
48 E. Elanthamilan and S. F. Wang, *J. Energy Storage*, 2025, **132**, 117738.
49 R. G. Bobade, N. B. Dabke, S. F. Shaikh, B. J. Lokhande, R. S. Mane and R. C. Ambare, *J. Energy Storage*, 2024, **84**, 110776.
50 D. Zheng, X. Sun, C. An, F. Pan, C. Qin, Z. Wang, Q. Deng, Y. Song and Y. Li, *Chem. Eng. J.*, 2023, **473**, 145289.
51 S. A. Thomas, J. Cherusseri, M. R. Pallavolu, M. Afzal and D. N. Rajendran, *Electrochim. Acta*, 2025, **522**, 145846.
52 J. A. Rajesh, J. Y. Park, S. H. Kang and K. S. Ahn, *Electrochim. Acta*, 2022, **414**, 140203.
53 R. N. Bulakhe, J. Lee, C. V. Tran and J. B. In, *J. Alloys Compd.*, 2022, **926**, 166864.
54 T. Keerthana, M. V. Arularasu, P. Mohanapriya, K. R. Bommisetti, M. M. Alam, A. G. Al-Sehemi and G. Ramalingam, *J. Mol. Struct.*, 2025, **1330**, 141493.
55 B. Jia, Y. Liu, X. Qiang, L. Wang, G. Zhao, S. Bai, H. Chen and X. Wu, *J. Colloid Interface Sci.*, 2025, **678**, 277–286.
56 Y. Cheng, K. Xia, H. Li, P. Liu, Z. Zhao, G. Xu, F. Wahid and H. Wang, *Colloids Surf., A*, 2023, **669**, 131544.
57 Y. Ping, H. Zhang and S. Meng, *Diamond Relat. Mater.*, 2025, **158**, 112694.
58 X. Zhou, C. Yang, J. Zhang, J. Chen, Y. Li, L. Lin, R. Jia and X. Xu, *J. Alloys Compd.*, 2025, **1031**, 180850.
59 S. AL-Rubaye, R. Rajagopalan, C. Subramaniyam, Z. Tai, J. Xian, X. Wang, S. X. Dou and Z. Cheng, *Dalton Trans.*, 2018, **47**, 14052–14059.
60 S. S. Scindia, R. B. Kamble and J. A. Kher, *AIP Adv.*, 2019, **9**, 55218.
61 E. Samuel, A. Aldalbahi, M. El-Newehy, H. El-Hamshary and S. S. Yoon, *J. Alloys Compd.*, 2021, **852**, 156929.
62 B. Senthilkumar, K. Vijaya Sankar, C. Sanjeeviraja and R. Kalai Selvan, *J. Alloys Compd.*, 2013, **553**, 350–357.
63 B. C. J. Mary, J. J. Vijaya, B. Saravanakumar, M. Bououdina and L. J. Kennedy, *Synth. Met.*, 2022, **291**, 117201.
64 J. Ge, G. Fan, Y. Si, J. He, H. Y. Kim, B. Ding, S. S. Al-Deyab, M. El-Newehy and J. Yu, *Nanoscale*, 2016, **8**, 2195–2204.
65 Y. Z. Cai, W. Q. Cao, Y. L. Zhang, P. He, J. C. Shu and M. S. Cao, *J. Alloys Compd.*, 2019, **811**, 152011.
66 S. B. Bandgar, M. M. Vadiyar, Y. C. Ling, J. Y. Chang, S. H. Han, A. V. Ghule and S. S. Kolekar, *ACS Appl. Energy Mater.*, 2018, **1**, 638–648.
67 Z. Y. Yu, L. F. Chen and S. H. Yu, *J. Mater. Chem. A*, 2014, **2**, 10889–10894.
68 B. Mordina, R. Kumar, N. S. Neeraj, A. K. Srivastava, D. K. Setua and A. Sharma, *J. Energy Storage*, 2020, **31**, 101677.
69 P. D. Patil, S. R. Shingte, V. C. Karade, J. H. Kim, T. D. Dongale, S. H. Mujawar, A. M. Patil and P. B. Patil, *J. Energy Storage*, 2021, **40**, 102821.
70 X. Zhang, Z. Zhang, S. Sun, Y. Wu, Q. Sun and X. Liu, *RSC Adv.*, 2018, **8**, 15222–15228.
71 Y. Zhang, W. Zhang, C. Yu, Z. Liu, X. Yu and F. Meng, *Ceram. Int.*, 2021, **47**, 10063–10071.
72 P. Nayak, S. K. Nayak and B. Satpathy, *Mater. Sci. Semicond. Process.*, 2022, **143**, 106543.
73 Z. Wang, X. Zhang, Y. Li, Z. Liu and Z. Hao, *J. Mater. Chem. A*, 2013, **1**, 6393–6399.
74 K. Hareesh, B. Shateesh, R. P. Joshi, S. S. Dahiwale, V. N. Bhoraskar, S. K. Haram and S. D. Dhole, *Electrochim. Acta*, 2016, **201**, 106–116.
75 M. B. Askari, P. Salarizadeh, Q. Guo, N. Chen and L. Qu, *Adv. Energy Sustainability Res.*, 2021, **2**, 27482–27491.
76 M. Fu, W. Chen, X. Zhu and Q. Liu, *J. Power Sources*, 2018, **396**, 41–48.
77 X. Gao, J. Bi, W. Wang, H. Liu, Y. Chen, X. Hao, X. Sun and R. Liu, *J. Alloys Compd.*, 2020, **826**, 154088.
78 N. Kumar, A. Kumar, G. M. Huang, W. W. Wu and T. Y. Tseng, *Appl. Surf. Sci.*, 2018, **433**, 1100–1112.
79 A. Soam, R. Kumar, P. K. Sahoo, C. Mahender, B. Kumar, N. Arya, M. Singh, S. Parida and R. O. Dusane, *ChemistrySelect*, 2019, **4**, 9952–9958.
80 Y. Zhao, L. Xu, J. Yan, W. Yan, C. Wu, J. Lian, Y. Huang, J. Bao, J. Qiu, L. Xu, Y. Xu, H. Xu and H. Li, *J. Alloys Compd.*, 2017, **726**, 608–617.